The morphology and distribution of Al_8Mn_5 in high pressure die cast AM50 and AZ91

G.Zeng[1*], X. Zhu[2], S. Ji[2], C.M. Gourlay[1*]

[1] Department of Materials, Imperial College London. SW7 2AZ. UK

[2] Brunel Centre for Advanced Solidification Technology (BCAST), Institute of Materials & Manufacturing, Brunel University London, Uxbridge, UB8 3PH, UK

* g.zeng@imperial.ac.uk
* c.gourlay@imperial.ac.uk
* Tel. +44 (0)20 7594 8707

Abstract

The morphology and distribution of Al_8Mn_5 is studied in AM50 and AZ91 produced by hot and cold chamber high pressure die casting (HPDC). It is found that, in HPDC, primary Al_8Mn_5 particles take a wide range of morphologies within the same casting spanning from faceted polyhedra to weakly-faceted dendrites. These different morphologies exist across the whole cross-section without any clear trend in morphology versus radial position. A comparison with Al_8Mn_5 in samples solidified at low cooling rate suggests that the larger polyhedral particles are externally solidified crystals (ESCs) that nucleate and grow in the shot chamber analogous to αMg ESCs, and that the dendritic Al_8Mn_5 nucleated and grew at high cooling rate in the die cavity.

Keywords HPDC, Externally solidified crystals, Porosity, Al_8Mn_5

Introduction

In recent years there has been a drive to use high pressure die casting (HPDC) for structural and crash-worthy automotive applications which has required improved HPDC quality through optimised melt handling, die design, process parameters and vacuum systems[1-3].

HPDC Mg components typically contain externally solidified αMg crystals (ESCs) which nucleate and grow in the shot chamber before being injected into the die cavity [4-6] The volume fraction of αMg ESCs is commonly 10-30 vol% and depends on the melt superheat and shot chamber characteristics including the fill fraction and the temperature of the sleeve walls and plunger tip[7, 8]. αMg ESCs are typically ~100 μm and are significantly larger than the in-cavity solidified αMg grain size of ~5-30 μm, leading to a bimodal grain size distribution[9]. The presence of larger αMg ESCs has been linked to a decrease in the mean elongation to fracture[10]and to an increased variability in ductility [11].

Most Mg-Al-based alloys contain a small Mn addition to ameliorate against the negative effects of Fe on corrosion resistance[12, 13]. Generally, AM, AZ, AS, and AE series alloys contain sufficient Al and Mn that Al_8Mn_5 is a primary phase (i.e. Al_8Mn_5 forms before αMg during solidification) as shown in Figure 1 [14] for the alloys used in this work (Table 1). A consequence of this in HPDC is that Al_8Mn_5 can form and settle in the holding pot/crucible (enhanced by Fe pick-up from the pot/crucible), leading to die casting sludge[15]. Furthermore, since Al_8Mn_5 forms at higher temperature than αMg, it might be expected that Al_8Mn_5 begins to form in the shot

chamber along with the externally solidified αMg crystals, and that the ESCs injected into the cavity are a mixture of Al_8Mn_5 and αMg.

This work was conducted to explore whether Al_8Mn_5 crystals form in the shot chamber and are injected into the cavity, and to understand how they are distributed in the final casting. Furthermore, this behaviour is compared in hot and cold chamber HPDC where the thermal conditions in the shot chamber / gooseneck are different and, therefore, the formation of ESCs is likely to be different.

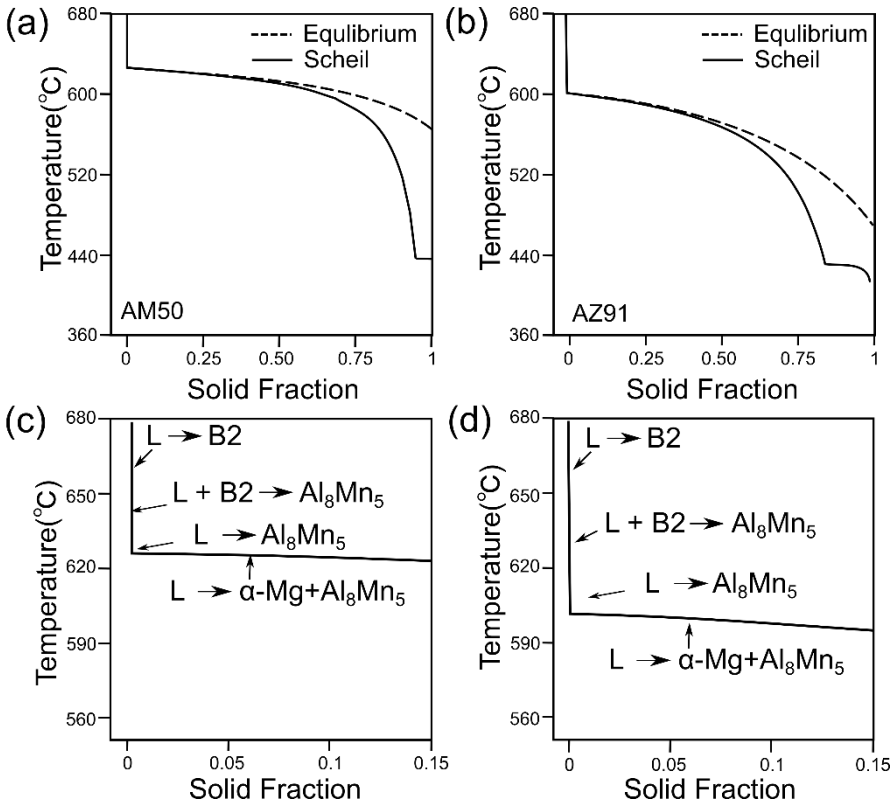

Figure 1: Scheil and equilibrium solidification paths of AM50 (a, c) and AZ91 (b,d) calculated with the Thermo-Calc TCMG4 database [14]. The top row shows the whole solidification path. The bottom row is a zoom-in on the beginning of solidification up to 15% solid fraction.

Methods

Mg alloys AM50 and AZ91 with compositions in Table 1 were used in this work. The AM50 steering wheel in Fig. 1(a) was produced industrially via the hot chamber HPDC process from the same die as in ref.[16]. The AZ91 tensile bar castings were produced by cold chamber HPDC on a 5 MN locking force Frech DAK 450-54. The multicavity die shown in Fig.1(b) was preheated to 150 °C. Liquid alloy at 675°C (~ 75°C superheat) was ladled into a preheated shot chamber. The plunger velocity was set to 0.3 ms^{-1} for the first phase and 4 ms^{-1} for the filling stage, and the intensification pressure was 36 MPa.

Samples for microstructural analysis were cut from the positions marked on Fig. 1 into slices of 10mm x 10mm x 0.5mm. Metallographic polishing was carried out down to 0.05µm colloidal silica by standard preparation methods. Samples were etched in a solution of 200ml ethylene glycol, 68ml distilled water, 4ml nitric acid and 80 ml acetic acid. A Zeiss AURIGA field emission gun SEM (FEG-SEM) with an Oxford Instruments INCA x-sight energy dispersive X-ray spectroscopy (EDX) detector and a BRUKER e-FlashHR electron backscatter

diffraction (EBSD) detector were used. Bruker ESPRIT 2.1 software was used to analyse the obtained EBSD patterns.

Table 1 AM50 and AZ91 alloy compositions

	Mg	Al	Zn	Mn	Si	Fe	Cu	Ni	ppm Be
AZ91E	Bal.	8.95	0.72	0.19	0.039	<0.001	0.001	<0.001	0.007
AM50	Bal.	4.79	0.007	0.23	0.011	<0.001	<0.002	0.001	\

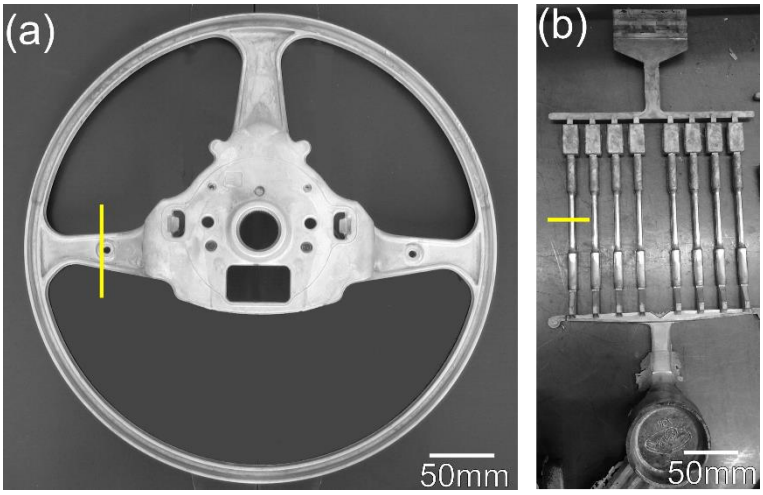

Figure 2: Photographs of the two castings. The position of the sectioning planes is indicated by the superimposed lines.

Results and Discussion

Al_8Mn_5 particles were identified by combining EDX with EBSD. A typical example is shown in Fig. 3 for the polyhedral particle marked with a cross in Fig. 3(a). The EDX spectrum in Fig. 3(b) contains no Mg peaks, indicating that the interaction volume did not contain any αMg matrix, and the composition 60.9Al-38.5Mn-0.6Fe (at%) is consistent with $Al_8(Mn,Fe)_5$. Fig. 3(c) shows an EBSD pattern collected from the same particle. The next image in Fig. 3(c) shows the pattern indexed as rhombohedral Al_8Mn_5 [17](with Strukturbericht designation $D8_{10}$) using the standard Hough transform method in BRUKER ESPRIT 2.2. To further confirm the phase, dynamical simulations were conducted in BRUKER DynamicS as shown in the right-most image of Fig. 3(c). It can be seen that there is good agreement in the band positions and band intensities between the experimental and dynamically simulated patterns. Thus, the particle is identified as Al_8Mn_5 with $D8_{10}$ structure by EDX and EBSD.

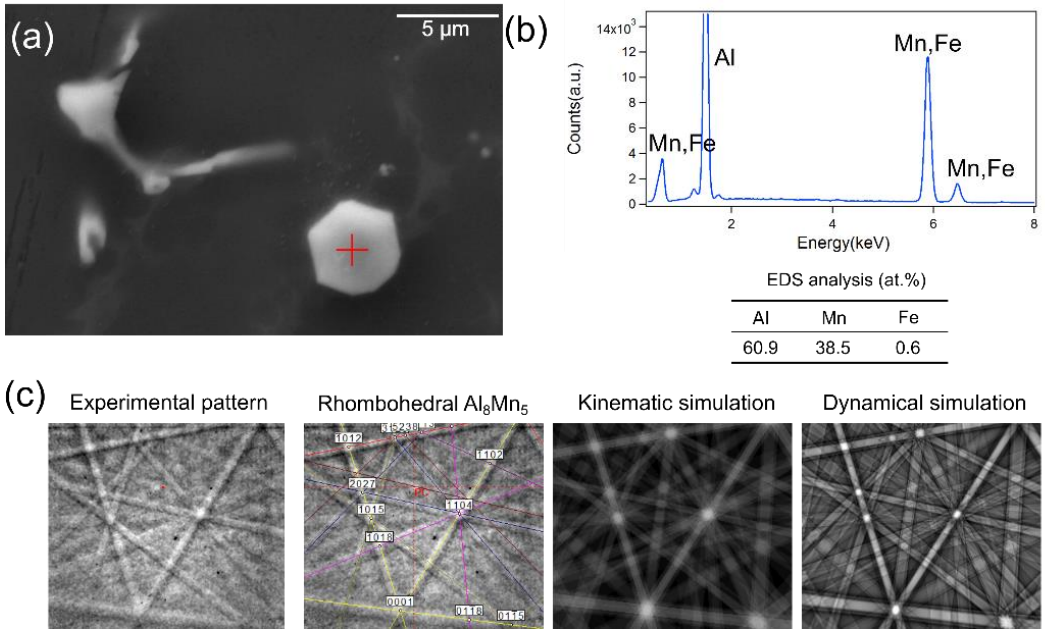

Figure 3 Phase analysis on Al-Mn particles by EDS and EBSD

Typical microstructures from the AM50 steering wheel are shown in Fig. 4 where the classical HPDC microstructural features are evident: The polished section in Fig. 4(a) and (c) contains two pore bands following the contour of the casting, similar to those discussed in past work [18-19]. After etching, Fig. 4(b) and (d) show αMg ESCs as well as the pore bands which appear as dark bands. The area fraction of αMg ESCs in this sample is ~5%, which is a low value for Mg HPDC. Higher magnification imaging of the pore bands in Fig. 4(f) shows that they contain a higher fraction of $Mg_{17}Al_{12}$ (i.e. more eutectic) than the surrounding regions, similar to past work [6]. In most regions of the casting, the Al_8Mn_5 appear as small particles that can be easily identified in backscattered electron (BSE) mode due to the much higher atomic-number of Mn compared with Mg and Al. For example, in Fig. 4(e), the numerous bright particles are Al_8Mn_5 and the lighter grey particles are $Mg_{17}Al_{12}$.

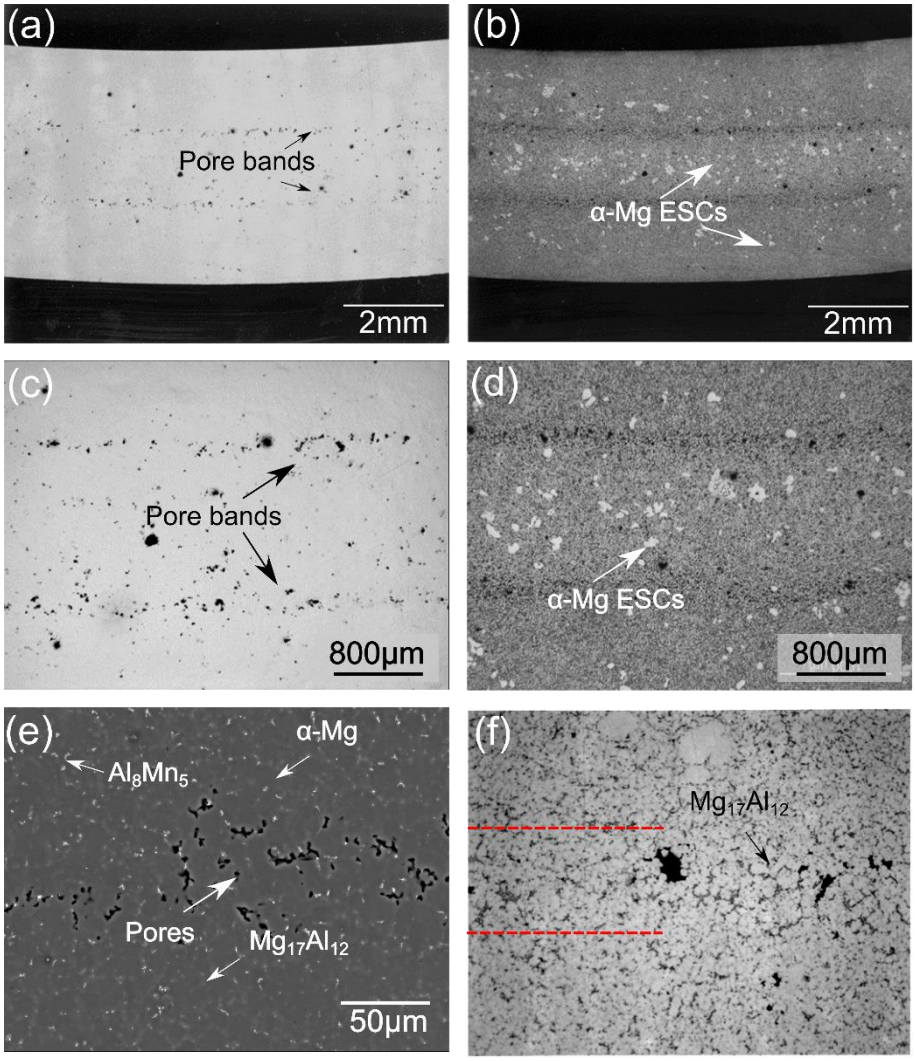

Figure 4: Macro- and microstructures of AM50 steering wheel. (a) and (c) as-polished sample optical micrograph showing the distribution of porosity. The bulk flow direction during HPDC was into the page(X). (b) and (d) etched-sample micrograph revealing the ESCs of α-Mg (white grains) and defects bands of macrosegregation. (e)BSE and (f) optical images of defect bands showing concentrated porosity and also fine eutectic $Mg_{17}Al_{12}$ network.

Al_8Mn_5 particles in the AM50 steering wheel are examined in more detail in Fig. 5. In low magnification BSE images (e.g. Fig. 5(a)) Al_8Mn_5 particles can be seen that have much larger size than the small Al_8Mn_5 particles present at higher magnification (e.g. in Fig. 4(e)). In Fig. 5(a), these larger Al_8Mn_5 particles are indicated with arrows. Fig. 5(b) examines a large Al_8Mn_5 particle at higher magnification. The Al_8Mn_5 particle is ~20μm long and has a faceted morphology. Adjacent, is a smaller particle (~2 μm across) with a similar composition that has a dendritic morphology and is, therefore, also expected to be primary Al_8Mn_5. It is likely that the smaller Al_8Mn_5 with dendritic morphology formed at significantly higher cooling rate than the large particle. To compare the two sizes of Al_8Mn_5 particle with the bimodal distribution of αMg grains, Fig. 5(c) shows that the αMg ESCs are an order or magnitude larger than the in-cavity solidified αMg grains. Based on the significantly different sizes of primary Al_8Mn_5 in Fig. 5(b) and the presence of αMg ESCs, it seems that the large Al_8Mn_5 particles in Fig. 5(a) and (b) are Al_8Mn_5 ESCs that nucleated and grew in the shot chamber or goose neck at low cooling rate before being injected into the die cavity, whereas the smaller primary Al_8Mn_5 nucleated and grew dendritically at higher

cooling rate. This interpretation will be further supported at the end of this paper when the size of large Al_8Mn_5 particles are shown to be similar to primary Al_8Mn_5 formed at low cooling rate.

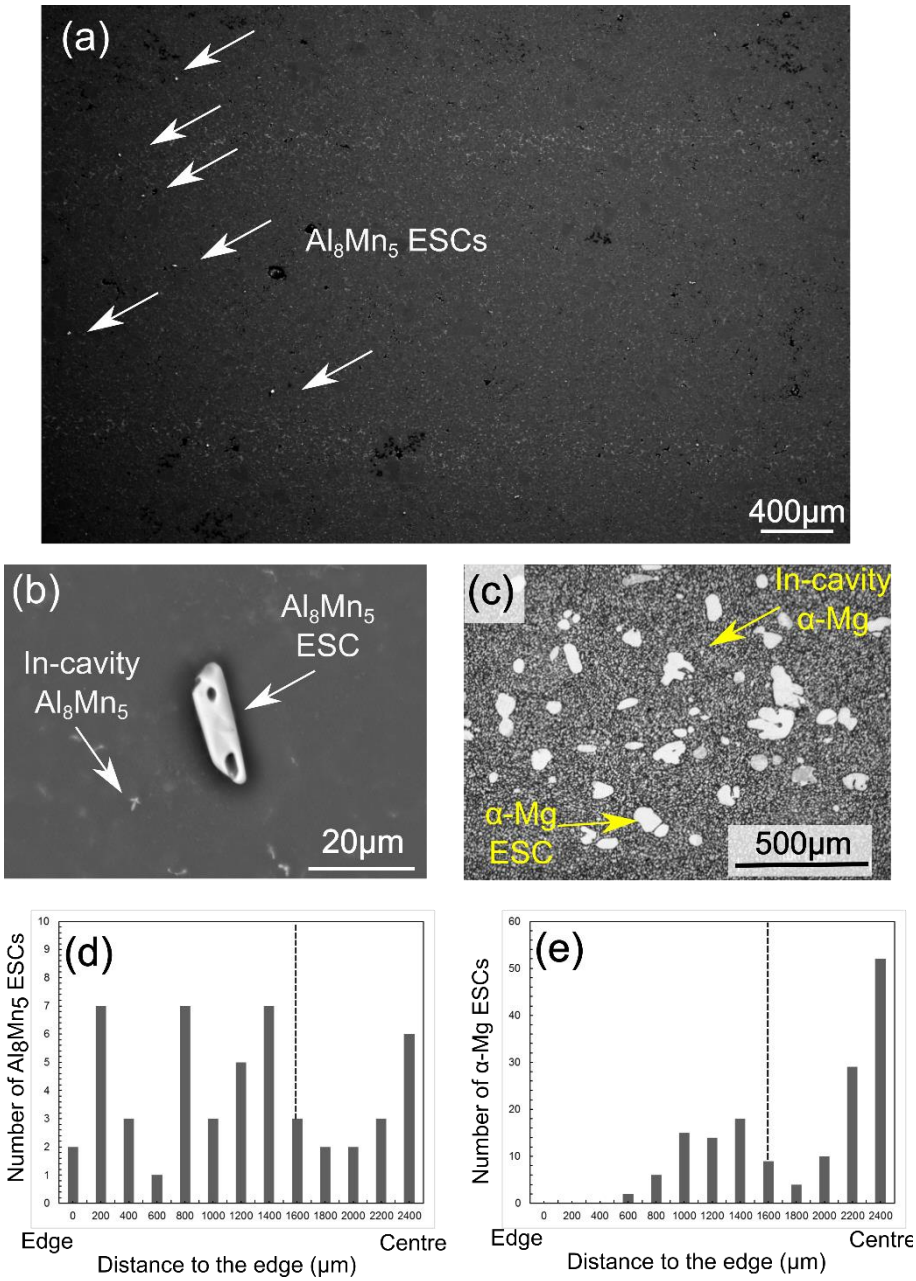

Figure 5: Distribution of ESCs of Al_8Mn_5 and α-Mg (a) BSE image at low magnification. (b) ESCs of Al_8Mn_5 and Al_8Mn_5 solidified in die cavity. Note the size different of two type of Al_8Mn_5 (c) ESCs of α-Mg (white grains). (e)

The distribution of large Al_8Mn_5 particles across the cross-section (i.e. vertically across Fig. 4(b)) is quantified in Fig. 5(d) and a similar quantification is shown for αMg ESCs in Fig. 5(e). It can be seen that there are more αMg ESCs near the centre and fewer near the edge of the cross-section similar to past work [5], while the large Al_8Mn_5 particles are distributed more uniformly across the cross-section. However, the total number of Al_8Mn_5 ESCs is low and the distribution in Fig. 5(d) should be treated with caution.

Typical microstructures from the AZ91 tensile bars are shown in Fig. 6. Similar to the steering wheel, there is a pore band following the contour of the casting (Fig. 6(a)). However, a significant difference is the much higher fraction of αMg ESCs in the cold chamber HPDC AZ91 tensile bars, estimated to be >30 vol%. This can be seen in Fig. 6(b) and (d) where αMg ESCs exist across most of the cross-section, either as large dendrites (Fig. 7(b)), coarsened flakes (Fig. 7(b)) or as ESC fragments (Fig. 6(d) and 7(b)). Examining Fig. 6(d), it can be seen that ESC fragments exist all the way to the casting edge. Fragmented and partially-globularised ESCs in cold chamber HPDC have been linked to the high shear rate during the filling stage in past work[20]. The high αMg ESC fraction and mixture of full ESC dendrites, ESC fragments and in-cavity solidified grains leads to a complex microstructure throughout the cross-section; for example, in Fig. 6(c), many ~50μm ESC αMg fragments can be seen surrounded by the smaller in-cavity solidified αMg grains.

Similarly, the AZ91 tensile bars contained a wide range of Al_8Mn_5 morphologies. A representative range is shown in Fig. 6(e)-(h): Fig. 6(e) has a faceted polyhedral morphology, Fig. 6(f)–(g) have complex branched morphologies with weaker faceting, and Fig. 6(h) are complex flakes. While the Al_8Mn_5 in Fig. 6(h) probably formed during a eutectic reaction, the faceted polyhedral particle in Fig. 6(a) and branched crystals in Fig. 6(f)–(g) are significantly larger than the surrounding eutectic intermetallics and are likely to be primary Al_8Mn_5. Some of the polyhedral Al_8Mn_5 particles were significantly larger than surrounding primary Al_8Mn_5 and are likely to be Al_8Mn_5 ESCs. Examples are given in Fig. 6(c) and Fig. 7(a) of polyhedral Al_8Mn_5 particles > 5 μm in diameter.

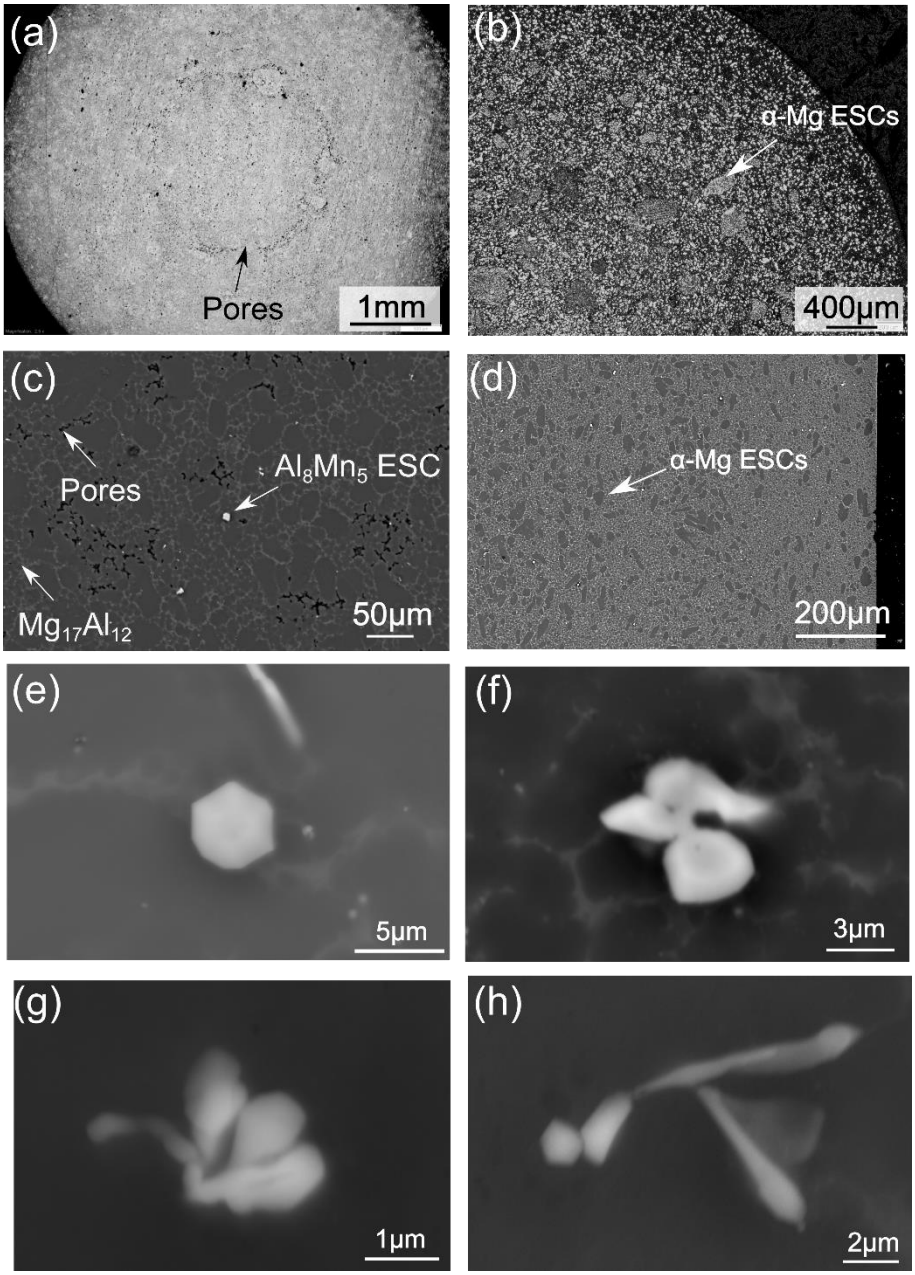

Figure 6: Transverse view of HPDC AZ91 tensile bar sample. (a) macrostructure showing defect bands. (b) etched microstructure and (d) BSE image shows macro-segregation and the ECSs of α- Mg grains. (c) BSE image at higher magnification shows pores, Al_8Mn_5 ECSs and eutectic $Mg_{17}Al_{12}$.

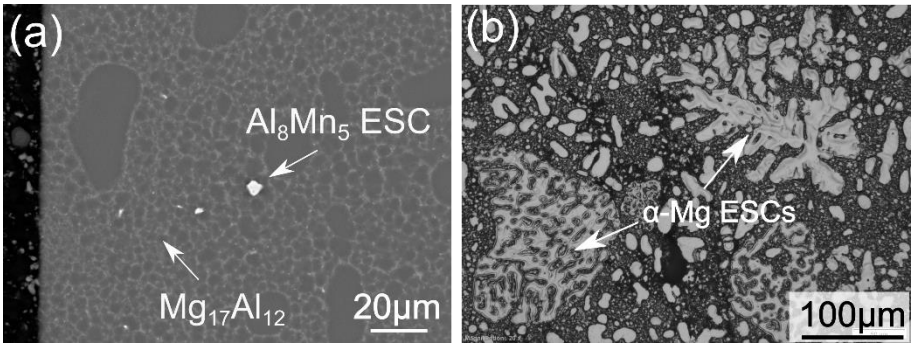

Figure 7: ESCs of (a) Al_8Mn_5 and (b) α- Mg grains surrounded by eutectic $Mg_{17}Al_{12}$/ α- Mg.

To further confirm that the larger polygonal Al_8Mn_5 are ESCs (i.e. formed in the gooseneck or shot sleeve/chamber before being injected into the cavity), Fig. 8 compares the large Al_8Mn_5 from HPDC with Al_8Mn_5 in AZ91 solidified at low cooling rate. Fig 8(a) are Al_8Mn_5 from the original AZ91 ingot (i.e. prior to melting and HPDC) and Fig. 8(c) are Al_8Mn_5 from AZ91 cooled at 1 K/s from the work in ref [21]. In both slow-cooled cases the primary Al_8Mn_5 have an equiaxed-polyhedral faceted morphology and a narrow size range [21] of ~5-15 μm. In Fig. 8(b) and (d) it can be seen that the large Al_8Mn_5 from the HPDC samples have a similar morphology and a similar size to those formed at low cooling rate in the laboratory. This, combined with the presence of a wide range of primary Al_8Mn_5 particles in HPDC including Al_8Mn_5 dendrites, shows that the larger polyhedral Al_8Mn_5 formed at lower cooling rate.

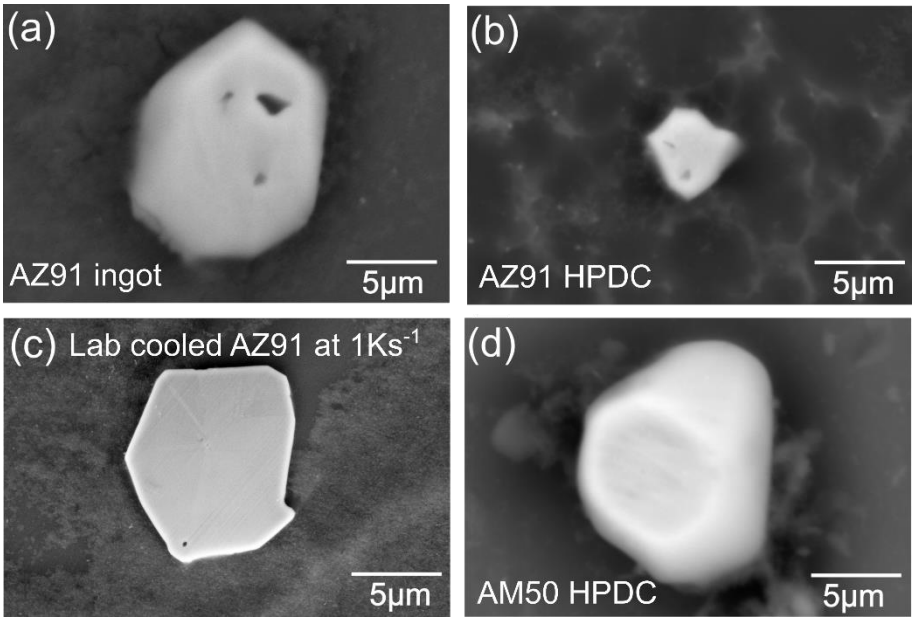

Figure 8 Faceted Al_8Mn_5 crystals in (a) AZ91 ingot, (b) HPDC AZ91, (c) AZ91 solidified at 1K/s and (d) AM50 steering wheel by HPDC.

The observation of both αMg and Al_8Mn_5 ESCs in AM50 and AZ91 high pressure die castings is consistent with the solidification paths predicted by Thermo-Calc with the TCMG4 database in Fig. 1, where B2-Al(Mn,Fe) and $D8_{10}$-Al_8Mn_5 are expected to form before αMg in the solidification sequence. Combining the microstructural

observations and thermodynamic calculations, it can be concluded that the largest polyhedral Al_8Mn_5 particles originally form in the shot chamber and are injected into the die cavity as a mixture of Al_8Mn_5, αMg and liquid.

The size of the largest Al_8Mn_5 particles in the casting is expected to be determined by the same factors that govern the size and volume fraction of αMg ESCs (melt superheat, fill fraction, thermal profile in the shot chamber, dwell time etc. [5]). Furthermore, since most commercial Mg-Al alloys (AM, AZ, AE, AJ etc.) contain sufficient Al and Mn for Al_8Mn_5 to be a primary phase, it is likely that Al_8Mn_5 ESCs will also form in the HPDC of these alloys. Al_8Mn_5 ESCs seem to be an integral part of the HPDC process of Mg-Al-based alloys and result in a small population of 5-20µm equiaxed-faceted Al_8Mn_5 crystals that are significantly larger than the in-cavity solidified Al_8Mn_5. However, Al-Mn particles form a very low volume fraction (~0.6 vol% [14]) and are rarely larger than 20µm even at low cooling rate.

Conclusions

Al_8Mn_5 particles have been studied in a hot chamber HPDC AM50 steering wheel and a cold-chamber HPDC AZ91 tensile bar casting. In both castings, polyhedral Al_8Mn_5 particles have been found to exist in the castings that have a similar morphology and size as primary Al_8Mn_5 formed in AZ91 at low cooling rate (~1 K s^{-1}). These polyhedral Al_8Mn_5 particles are significantly larger than the branched primary Al_8Mn_5 in the same HPDC cross-sections. It is concluded that the large polyhedral Al_8Mn_5 particles nucleated and grew in the shot chamber along with the αMg externally solidified crystals (ESCs) and were injected into the die cavity as a mixture of Al_8Mn_5, αMg and liquid. This interpretation is supported by thermodynamic calculations with the Thermo-Calc TCMG4 database which predicts that primary Al_8Mn_5 should begin to form at higher temperature than αMg and, therefore, that a mixture of primary Al_8Mn_5 and αMg externally solidified crystals (ESCs) should exist in the shot sleeve when pre-solidification occurs. Partial solidification in the shot chamber followed by in-cavity solidification at higher cooling rate leads to a wide range of primary Al_8Mn_5 morphologies in the same cross section, spanning from large (≤20 µm) polyhedral particles to significantly smaller branched primary crystals.

Acknowledgments

Financial support from EPSRC (UK) under grant number EP/N007638/1 is gratefully acknowledged.

References

[1] Luo AA (2013) Magnesium casting technology for structural applications. Journal of Magnesium and Alloys 1(1):2-22.

[2] Wang QL, Xiong SM (2015) Effect of multi-step slow shot speed on microstructure of vacuum die cast AZ91D magnesium alloy. Transactions of Nonferrous Metals Society of China 25(2):375-380.

[3] Ji S, Yang W, Jiang B, Patel J, Fan Z (2013) Weibull statistical analysis of the effect of melt conditioning on the mechanical properties of AM60 alloy. Mater. Sci. Eng., A 566:119-125.

[4] Bowles A, Griffiths J, Davidson C (2001) Ductility and the Skin Effect in High Pressure Die Cast Mg-Al Alloys. Magnesium Technology 2001:161-168.

[5] Laukli H, Lohne O, Sannes S, Gjestland H, Arnberg L (2003) Grain size distribution in a complex AM60 magnesium alloy die casting. Int. J. Cast Met. Res. 16(6):515-521.

[6] Gourlay C, Laukli H, Dahle A (2007) Defect band characteristics in Mg-Al and Al-Si high-pressure die castings. Metall. Trans. A 38(8):1833-1844.

[7] Laukli H, Graciotti A, Lohne O, Gjestland H, Sannes S (2002) The effect of solidification of metal prior to injection in HPDC on the grain size distribution in a complex die casting. NADCA Transactions 21(T02-035):1-4.

[8] Bi C, Xiong S, Li X, Guo Z (2016) Development of a Fluid-Particle Model in Simulating the Motion of External Solidified Crystals and the Evolution of Defect Bands in High-Pressure Die Casting. Metall. Trans. B 47(2):939-947.

[9] Bowles A, Nogita K, Dargusch M, Davidson C, Griffiths J (2004) Grain size measurements in Mg-Al high pressure die castings using electron back-scattered diffraction (EBSD). Mater. Trans., JIM 45(11):3114-3119.

[10] Easton M, Abbott TB, Cáceres CH, The effect of microstructural features and defects on the ductility of high pressure die cast AS21, AM60 and AZ91. Materials Science Forum 147-152.

[11] Gjestland H, Sannes S, Svalestuen J, Westengen H, Optimizing the magnesium die casting process to achieve reliability in automotive applications. SAE Technical Paper, 2005.

[12] Hanawalt JD, Holdeman GE, Nelson CE, Removal of iron from magnesiumbase alloys, US. Patent 2.267.862 December 1941.

[13] Liu M, Uggowitzer PJ, Nagasekhar AV, Schmutz P, Easton M, Song G-L, Atrens A (2009) Calculated phase diagrams and the corrosion of die-cast Mg–Al alloys. Corros. Sci. 51(3):602-619.

[14] Thermo-Calc. TCMG Database version 4.0, 2015.

[15] Corby C, Ricketts N, Qian M (2004), Investigation of intermetallics in magnesium die-casting sludge, Magnesium Technology 2004: 209-214.

[16] Otarawanna S, Gourlay C, Laukli H, Dahle A (2009) The thickness of defect bands in high-pressure die castings. Mater. Charact. 60(12):1432-1441.

[17] Ellner M (1990) The structure of the high-temperature phase MnAl(h) and the displacive transformation from MnAl(h) into Mn5Al8. Metall. Trans. A 21:1669-1672.

[18] Gourlay CM, Meylan B, Dahle AK (2008) Shear mechanisms at 0-50% solid during equiaxed dendritic solidification of an AZ91 magnesium alloy. Acta Mater. 56:3403-3413.

[19] Gourlay CM, Dahle AK, Laukli HI (2004) Segregation band formation in Al-Si die castings. Metall. Trans. A 35(9):2881-2891.

[20] Ghomashchi M (1995) High-pressure die casting: effect of fluid flow on the microstructure of LM24 die-casting alloy. J. Mater. Process. Technol. 52(2-4):193-206.

[21] Zeng G, Xian JW, Gourlay CM (2017) Growth of Al_8Mn_5 Intermetallic in AZ91, Magneisum Techmology 2017:85-92.